Extreme-ultraviolet spectroscopy of highly charged xenon ions created using an electron-beam ion trap

K. Fahy,[1] E. Sokell,[1] G. O'Sullivan,[1] A. Aguilar,[2,*] J. M. Pomeroy,[2] J. N. Tan,[2] and J. D. Gillaspy[2]
[1]*School of Physics, University College Dublin, Belfield, Dublin 4, Ireland*
[2]*National Institute of Standards and Technology, Gaithersburg, Maryland 20899, USA*
(Received 28 October 2006; published 27 March 2007)

Extreme-ultraviolet spectra of xenon ions have been recorded in the 4.5 to 20 nm wavelength region using an electron beam ion trap and a flat field spectrometer. The electron beam energy was varied from 180 eV to 8 keV and radiation from charge states Xe^{6+} to Xe^{43+} was observed. Our measured wavelengths were compared to atomic structure calculations using the Cowan suite of codes. We have measured seventeen previously unreported features corresponding to transitions in Xe^{35+} through to Xe^{41+} with estimated wavelength uncertainties of ±0.003 nm. It was found that for the case of continuous injection of neutral xenon gas a wide range of charge states were always present in the trap but this charge state distribution was greatly narrowed, towards higher charge states, if a sufficiently low gas injection pressure was employed. The energy dependence of spectral lines arising from Xe^{42+} and Xe^{43+} revealed enhancement of the total ionization cross sections, due to excitation-autoionization of $n=2$ electrons to $n=3$ levels, in the Xe^{41+} and Xe^{42+} charge states.

DOI: 10.1103/PhysRevA.75.032520 PACS number(s): 32.30.Jc, 34.80.Dp

I. INTRODUCTION

It is well known that xenon ions produced under high temperature plasma conditions emit strongly in the extreme-ultraviolet (EUV) spectral range. The EUV spectrum of xenon arising from charge states Xe^{6+} to Xe^{10+} has been well documented due to observations of vacuum discharge plasmas and laser-produced plasmas [1–8]. Xenon has recently been earmarked as a possible source for EUV lithography due to radiation arising from the $4d$-$5p$ transition array in the Xe^{10+} ion, centered at 13.5 nm [5,9,10]. The charge states Xe^{11+} through to Xe^{17+} produce strong emission from $4d$-$4f$ transitions that overlap in energy to produce an unresolved transition array (UTA) [11–15], centered near 11 nm. Radiation from this transition array was observed previously at the National Institute of Standards and Technology Electron Beam Ion Trap (NIST EBIT) and has been reported elsewhere [16].

EUV radiation from highly charged xenon ions has been observed in EBIT spectra by other groups as well. Träbert *et al.* [17] have reported wavelengths of prominent lines arising from $3s$-$3p$ transitions in Xe^{42+} and Xe^{43+} as well as lines from *B*-like, Be-like, and Li-like xenon ions. Träbert *et al.* [17] measured the $3s^2\ ^1S_0$-$3s3p\ ^1P_1$ and $3s\ ^2S_{1/2}$-$3p\ ^2P_{3/2}$ spectral lines of Xe^{42+} and Xe^{43+}, respectively, using an electron beam energy of 20 keV, while spectral lines from higher charge states up to Li-like were measured using a beam energy of 133 keV. All these lines were observed in the 4 nm to 20 nm wavelength region, which is very similar to the wavelength range studied in this work. In their experiments, neutral xenon gas was continually injected into the trap region by means of a ballistic gas injector. Biedermann *et al.* [18] have studied the spectral range between 9 and 25 nm and they observed lines from $4p$-$4d$ transitions in ions Xe^{17+} through to Xe^{20+}, lines from $4p$-$4d$ and $4s$-$4p$ transitions in Xe^{21+} to Xe^{23+} as well as the well known $4s$-$4p$ transitions in Xe^{24+} and Xe^{25+}. Neutral xenon was continually fed into the trap region and the electron beam energy was varied from 434.2 eV for the Xe^{17+} spectrum up to 855.5 eV for the Xe^{25+} spectrum. Biedermann *et al.* [18] compared their wavelengths and intensities to those calculated by the HULLAC suite of codes [19].

At the NIST EBIT we have trapped and observed radiation from a wide range of xenon charge states as the electron beam energy was tuned from 180 eV up to 8 keV. As the electron beam energy was increased above the ionization threshold to produce a particular ion, we could observe emission from that ion stage. Spectra obtained at successive electron beam energies were overlaid and we compared the spectral features with published line lists as well as with atomic structure calculations performed at University College Dublin using the Cowan suite of codes. The result is a listing of emission lines from ions Xe^{6+} up to Xe^{43+} between 4.5 and 20 nm, including wavelengths, observed relative intensities, and some identifications along with a presentation of the relevant spectra. A total of forty seven spectra, taken under different conditions, were analyzed in this work.

II. EXPERIMENT

The EBIT is a versatile source capable of producing nearly any ion charge state [20]. It consists of a tightly focused electron beam that serves to create, trap, and excite highly charged ions. The electron beam energy is tunable, thus allowing good charge state selectivity. A superconducting Helmholtz-pair magnet provides a 3 T axial magnetic flux density that compresses the electron beam to a radius of about 30 μm. The electron beam is accelerated through a set of three copper electrodes or drift tubes, the outer two held at a positive potential with respect to the inner one. Neutral gas is then injected into the middle drift tube region where the ions are formed by interaction with the electron beam. The

*Present address: Advanced Light Source, Lawrence Berkeley National Laboratory, Berkeley, CA 94720, USA.

positive ions are then trapped by a combination of the negative space charge of the electron beam, the axial potential well formed by the drift tubes, and the axial magnetic field. In the trapping region, the electron beam energy is determined by the potential applied to the middle drift tube.

After collisional excitation with the electron beam the radiation emitted from the plasma is viewed through a side window orientated at 90° to the electron beam direction. A flat field EUV spectrometer [21], based on the design of Kita *et al.* [22] was used in this work. This instrument has a very efficient light gathering capability while maintaining a high resolution. The EUV spectrometer was employed in this work to obtain spectra of xenon in the 4.5–20 nm range. The resolution of the spectrometer varies from 0.02 nm at 4 nm to 0.035 nm at 20 nm. Wavelength calibration was first performed by determining the central position (in pixels) of a number of well known transitions of xenon, argon, and neon ions injected into the EBIT at an electron beam energy of 8 keV, and then fitting a fourth-order polynomial to the calibration data. This calibration procedure along with a detailed list of the calibration lines used is presented in [21]. This calibration was applied to the spectra presented in Secs. IV A–IV D with the wavelength accuracy estimated to be ±0.02 nm across the spectral range. An improved calibration was obtained for the high energy data presented in Sec. IV E. This was done by using seven well known lines in the xenon spectrum. A Gaussian function was fitted to each line and its noninteger pixel center was found. This procedure was repeated for six different xenon frames taken on the same day and the collective statistical weight of the line positions were used to fit a dispersion function which could be applied to all xenon frames taken under the same EBIT operating conditions. This calibration was applied to the spectra presented in Sec. IV E giving an estimated accuracy of ±0.003 nm. The detector used was a liquid nitrogen cooled, back-illuminated CCD consisting of an array of 1340 (horizontal) ×400 (vertical) pixels, operated in the spectroscopy mode. The spectroscopy mode allows binning of the 400 vertical pixels into a one-dimensional row of 1340 pixels, resulting in improved signal to noise ratios. The spectra were corrected for cosmic ray events in postacquisition and typical integration times ranged from 3 to 30 min. All line intensities plotted or tabulated in this paper have been corrected for the spectrometer response function [21].

Xenon gas was injected continuously, typically at injector reservoir pressures of 6.7×10^{-3} to 1.2×10^{-2} Pa. During one particular experimental run, the gas injection pressure was lowered to 9.3×10^{-6} Pa. It should be noted that the gas pressure in the trap region is expected to be less than 10^{-9} Pa, for even the highest gas injection pressures employed. The pressure in the EBIT is much lower than that in the gas injector because the two are separated by a small tube, which limits the pumping speed on the gas chamber to much lower values than that provided to the EBIT chamber by its pumps (see Appendix for details of the gas injector setup). During acquisition of spectra for electron beam energies of 180 to 500 eV, the middle drift tube was biased at a constant potential of −100 V, relative to the two end electrodes. In all subsequent runs at electron beam energies greater than 500 eV, the middle drift tube was biased at −500 V relative to the end electrodes. The electron beam current was maximized at each value of beam energy.

Although the electron beam energy is determined by the center drift tube potential, the exact energy is somewhat less than this due to beam space charge defects. The electron beam space charge correction V_{sc} to the beam energy in EBIT is given, in eV, by $V_{sc}\sim-5I_{beam}/E_{beam}^{1/2}$ [23], where I_{beam} is the beam current in mA at energy E_{beam}, given in keV. For example, with a 8 keV, 130 mA electron beam, the magnitude of this correction is ∼−240 eV. This is an upper bound since V_{sc} does not contain the positive space charge of the trapped ions. The beam energies E_{beam} as quoted in Sec. IV of this paper have not been space charge corrected.

III. THEORY

The Hartree-Fock (HF) approximation with the Cowan code [24] was used to calculate theoretical spectra of transition probability (gA value) versus wavelength (λ) for a range of xenon ions, from Xe^{6+} to Xe^{46+}. The theoretical spectral lines were convolved with a Gaussian function of full width at half maximum appropriate to our flat field spectrometer resolution at that wavelength. The Gaussian functions were then summed to produce the theoretical spectrum for that ion stage. The resulting theoretical spectra were compared to the spectra obtained at successive beam energies and were used to aid the identification of spectral features in the experimental spectra. It should be noted that the calculations did not include optically forbidden transitions and generally only transitions from the ground state were included. Also, the population of the emitting level can be an important factor in the interpretation of EBIT data, and this may have more bearing on the observed line intensity than the gA value.

In order to optimize the output from the Cowan code, the Slater-Condon integrals (F^k,G^k,R^k) and spin-orbit integral (ζ) were adjusted to match the Cowan wavelengths to the previously reported wavelengths listed in Table I. The F^k,G^k,R^k integrals were adjusted *en bloc* with the spin-orbit integral adjusted separately. The ion stages Xe^{8+} to Xe^{17+} contain a $4d$ electron in their valence subshell and their spectra are dominated by $4d$-$4f$ transitions. Figure 1 shows the result of varying F^k,G^k,R^k from 70% to 90% of the HF value in the calculation of the Xe^{8+} spectrum. ζ was adjusted separately and a value of 99% of the HF value was found to be optimum. The well known $4d^{10}$-$4d^9 4f\ {}^1S_0$-$^1P_1$ line of Xe^{8+}, reported by Churilov and Joshi [4], was used as the reference line and the absolute error between theory and experiment was calculated for each set of F^k,G^k,R^k. A minimum error of 0.09 nm was obtained with $F^k,G^k,R^k=79\%$ and $\zeta=99\%$ for this line. The excited configurations included in the Xe^{8+} spectrum were $4d$-nf ($n=4-8$), $4d$-np ($n=5-8$), $4p$-nd ($n=5,6$), and $4p$-ns ($n=5,6$) and transitions to the ground state ($4d^{10}$) were calculated. The values of $F^k,G^k,R^k=80\%$ and $\zeta=99\%$ were found to best match the $4d$-$4f$ reported wavelengths for Xe^{9+} and Xe^{10+} ions and these values were used to calculate theoretical spectra for the ion stages up to Xe^{17+}. For higher ion stages up to Xe^{37+} the scaling factors of $F^k,G^k,R^k=90\%$ and $\zeta=99\%$ were found to yield the most accurate results. The scaling factors required

TABLE I. Theoretical and experimental spectral lines of Xe^{6+} to Xe^{9+} observed at the NIST EBIT at an electron beam energy of 180 eV. Observed intensities relative to the most intense line (Xe^{8+} $4d^{10}$-$4d^9 4f\ ^1S_0$-$^1P_1$ [4]) are listed in column 5 while column 8 lists the experimental wavelengths obtained by other authors. The Xe^{9+} 4*d*-5*p* transition array between 14 and 15 nm was also observed, individual features of which are omitted from this table.

Ion	Lower level	Upper level	NIST EBIT λ[b] (nm)	NIST EBIT Rel. Int.	Cowan[a] λ (nm)	Cowan[a] gA (10^{10} s^{-1})	Reported λ (nm)
Xe^{8+}	$4d^{10}\ ^1S_0$	$4d^9 6f\ ^1P_1$	8.54	0.03	8.54	34	8.5420[c]
Xe^{8+}	$4d^{10}\ ^1S_0$	$4d^9 7p\ ^3P_1$	8.85	0.02	8.85	7	8.8444[c]
Xe^{8+}	$4d^{10}\ ^1S_0$	$4d^9 5f\ ^1P_1$	9.63	0.13	9.61	140	9.6449[c]
Xe^{8+}	$4d^{10}\ ^1S_0$	$4d^9 6p\ ^1P_1$	10.28	0.02	10.29	12	10.2815[c]
Xe^{8+}	$4d^{10}\ ^1S_0$	$4d^9 6p\ ^3P_1$	10.38	0.02	10.39	9	10.3808[c]
Xe^{9+}	$4d^9\ ^2D_{5/2}$	$4d^8 4f\ (\mathbf{887203})_{5/2}$[d]	11.29	0.02	11.29	12	11.2714[c]
Xe^{9+}	$4d^9\ ^2D_{5/2}$	$4d^8 4f\ (\mathbf{881539})_{3/2}$[d]	11.35	0.03	11.32	441	11.3438[c]
Xe^{9+}	$4d^9\ ^2D_{5/2}$	$4d^8 4f\ (\mathbf{874794})_{3/2}$[d]	11.43	0.08	11.44	295	11.4312[c]
Xe^{9+}	$4d^9\ ^2D_{3/2}$	$4d^8 4f\ (\mathbf{887203})_{5/2}$[d]	11.49	0.47	11.50	1070	11.4880[c]
Xe^{9+}	$4d^9\ ^2D_{5/2}$	$4d^8 4f\ (\mathbf{870470})_{7/2}$[d]			11.49	1450	11.4880[c]
Xe^{9+}	$4d^9\ ^2D_{3/2}$	$4d^8 4f\ (\mathbf{881539})_{3/2}$[d]	11.57	0.30	11.53	288	11.5632[c]
Xe^{9+}	$4d^9\ ^2D_{5/2}$	$4d^8 4f(\mathbf{864592})_{5/2}$[d]			11.59	982	11.5661[c]
Xe^{8+}	$4d^{10}\ ^1S_0$	$4d^9 4f\ ^1P_1$	12.02	1	12.00	456	12.0133[c]
Xe^{7+}	$5s\ ^2S_{1/2}$	$4d^9 5s4f\ ^2P_{3/2}$	12.32	0.31	12.56	563	12.3243[c]
Xe^{7+}	$5s\ ^2S_{1/2}$	$4d^9 5s4f\ ^2P_{1/2}$			12.56	282	12.3265[c]
Xe^{6+}	$5s^2\ ^1S_0$	$4d^9 5s^2 4f\ ^1P_1$			12.19	186	12.3242[e]
Xe^{8+}	$4d^{10}\ ^1S_0$	$4d^9 4f\ ^3D_1$	14.36	0.04	14.31	0.6	14.3614[c]
Xe^{8+}	$4d^{10}\ ^1S_0$	$4d^9 5p\ ^3D_1$	16.18	0.06	16.15	25	16.1742[c]
Xe^{8+}	$4d^{10}\ ^1S_0$	$4d^9 5p\ ^1P_1$	16.53	0.26	16.50	4	16.5323[c]
Xe^{7+}	$5s\ ^2S_{1/2}$	$4d^9 5s5p(5/2,{}^1P_1)_{3/2}$[f]	17.09	0.08	17.09	16	17.0856[g]
Xe^{7+}	$5s\ ^2S_{1/2}$	$4d^9 5s5p(3/2,{}^3P_2)_{1/2}$[f]	17.60	0.08	17.61	0.7	17.5872[g]
Xe^{7+}	$5s\ ^2S_{1/2}$	$4d^9 5s5p(3/2,{}^3P_1)_{1/2}$[f]	17.73	0.05	17.76	10	17.7258[g]
Xe^{7+}	$5s\ ^2S_{1/2}$	$4d^9 5s5p(3/2,{}^3P_1)_{3/2}$[f]	17.78	0.06	17.78	14	17.7707[g]
Xe^{7+}	$5s\ ^2S_{1/2}$	$4d^9 5s5p(3/2,{}^3P_0)_{3/2}$[f]	17.98	0.02	17.92	2	17.9656[g]
Xe^{7+}	$5s\ ^2S_{1/2}$	$4d^9 5s5p(3/2,{}^3P_0)_{3/2}$[f]	18.15	0.02	18.07	0.5	18.1670[g]
Xe^{6+}	$5s^2\ ^1S_0$	$4d^9 5s^2 5p\ ^3D_1$	18.21	0.02	18.19	3	18.1876[e]
Xe^{7+}	$5s\ ^2S_{1/2}$	$4d^9 5s5p(5/2,{}^3P_1)_{3/2}$[f]	18.44	0.09	18.31	1	18.4655[g]
Xe^{6+}	$5s^2\ ^1S_0$	$4d^9 5s^2 5p\ ^1P_1$	18.56	0.09	18.55	18	18.5438[e]

[a]Scaling factors of F^k, G^k, R^k=80% and ζ=99% were used in the calculations.
[b]The estimated uncertainty of the wavelengths measured at NIST in this table is ±0.02 nm.
[c]Churilov and Joshi [4].
[d]Numbers in boldface represent the values of the excited configuration energy levels (in cm^{-1}) as listed by Churilov and Joshi [4].
[e]Kaufman and Sugar [2].
[f]In [3] the $4d^9\ ^2D_{J_1}$ level was coupled to $5s5p\ ^{1,3}P_{J_2}$ to form the final *J* state. The first term in brackets, e.g., $(5/2,{}^1P_1)_{3/2}$ represents the J_1 term with the second term representing the $^{1,3}P_{J_2}$ term. The subscript outside of the brackets denotes the final *J* state.
[g]Kaufman and Sugar [3].

for the ion stages of Xe^{38+} to Xe^{43+} were values of F^k, G^k, R^k=95% and ζ=99%. The scaling factors of 90% to 95% used in the calculation of the spectra for ion stages $>Xe^{17+}$ are consistent with the value of 93% used by Morgan *et al.* [25] in their calculation of the Xe^{32+} $3d^4\ ^5D_2$-$^5D_3$ and the Ba^{34+} $3d^4\ ^5D_2$-$^5D_3$ ultraviolet or visible lines, and points to the general trend that the required percentage adjustment of the scaling factors becomes less with increasing ion stage. Also, it seems this general trend remains true across the visible, ultraviolet, and EUV spectral regimes.

Figure 2(a) shows a comparison between our calculations and experiment for the 3*p*-3*d* transitions of the Xe^{28+} ion as measured by Wyart *et al.* [26]. They used a tokamak as their light source and the quoted uncertainty of their wavelength measurements is 0.002 nm. Our calculations are shown (dashed line) to underestimate their line positions by a mean

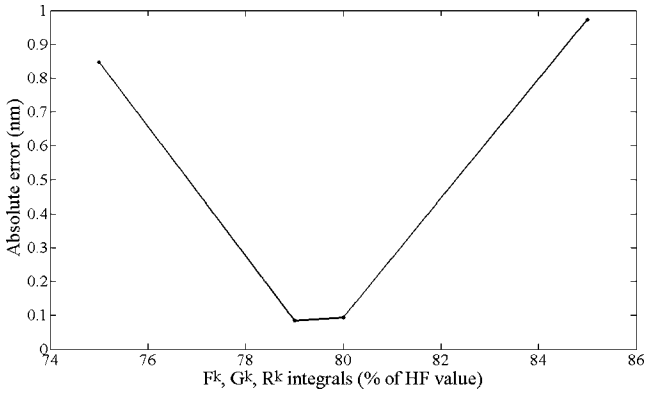

FIG. 1. Comparison of calculated line position with known line position for the Xe^{8+} $4d^{10}$-$4d^9 4f$ $^1S_0$-$^1P_1$ transition at 12.0133 nm [4]. The Slater integrals F^k, G^k, R^k were adjusted *en bloc* until the absolute error between theory and experiment was a minimum. The spin-orbit integral, ζ, was held at its optimum value of 99% of the HF value.

of 0.033 nm. Figure 2(b) compares our theoretical calculations for the $4s$-$4p$ transitions of Xe^{21+} to Xe^{23+} to the prominent features of the same transitions observed in EBIT, with a quoted uncertainty of 0.0058 nm, by Biedermann *et al.* [18]. Our calculations are seen (dashed line) to overestimate their line positions by a mean of 0.05 nm. Similarly, our calculations for the $3s^2$ $^1S_0$-$3s3p$ $^1P_1$ line of Xe^{42+} and the $3s$ $^2S_{1/2}$-$3p$ $^2P_{3/2}$ line of Xe^{43+} agree with Träbert *et al.* [17] measurements (6.2875±0.0012 nm and 6.6574±0.0020 nm) to within 0.063 nm and 0.011 nm, respectively. Consequently, in the majority of cases, we feel confident in our Cowan calculations, to at least the 0.1 nm level of accuracy, and we have quoted our calculated wavelength values to one additional decimal point.

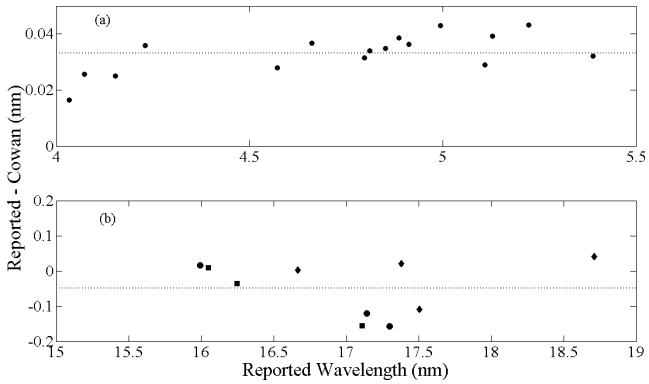

FIG. 2. Comparison of our Cowan calculations with experimentally known line positions from highly charged xenon. The above figure represents the difference between experiment and calculation for (a) the $3p$-$3d$ transitions of Xe^{28+} and (b) the $4s$-$4p$ transitions of Xe^{21+} (♦), Xe^{22+} (●), and Xe^{23+} (■). The dashed lines in both plots represent the mean difference between our theoretical wavelengths and the experimental wavelengths of [18,26]. The $3p$-$3d$ transitions are underestimated by 0.033 nm while the $4s$-$4p$ transitions are too large by a mean of 0.05 nm. Scaling factors of F^k, G^k, R^k=90% and ζ=99% were used in the calculations.

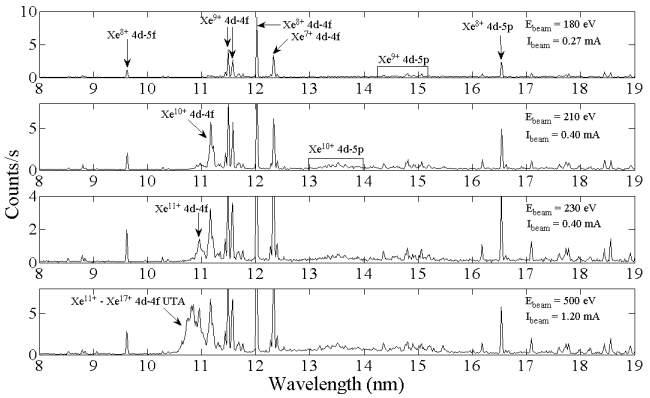

FIG. 3. Spectra obtained at electron beam energies of 180 to 500 eV and a gas injection pressure of 1.2×10^{-2} Pa. The strongest feature in each of the above spectra is the Xe^{8+} $4d^{10}$-$4d^9 4f$ $^1S_0$-$^1P_1$ transition at 12.02 nm [4]. The electron beam energy (E_{beam}) and current (I_{beam}) are listed in the figure for each spectrum. The 210 to 500 eV spectra are truncated to clearly show the labeled features. The identification of the lines observed at the electron beam energy of 180 eV are given in Table I.

IV. LINE SPECTRA AND ANALYSIS

A. 180 to 500 eV line spectra

Figure 3 shows the spectra obtained with electron beam energies of 180 to 500 eV at a gas injection pressure of 1.2×10^{-2} Pa. In each of these spectra the most intense line observed was the Xe^{8+} $4d$-$4f$ $^1S_0$-$^1P_1$ transition at 12.02 nm, previously reported at 12.0133 nm [4]. At 180 eV emission from ion stages Xe^{6+} to Xe^{9+} was observed. The spectral lines arising from these ion stages are well documented and Table I lists the features observed in the present work. At an electron beam energy of 210 eV the Xe^{10+} ion (produced at 202 eV) is present in the trap and we observed the $4d$-$4f$ and $4d$-$5p$ transition arrays centered at 11.17 and 13.51 nm, respectively. The spectrum at 230 eV shows an additional feature peaked at 10.96 nm which is $4d$-$4f$ emission arising from the Xe^{11+} ion, predicted by our theoretical spectrum to peak at a wavelength of 10.97 nm. The energy required to produce Xe^{11+} is 227 eV. All xenon ionization energies were taken from [27].

At the electron beam energy of 500 eV (at which the maximum charge state attainable was Xe^{17+}) the $4d$-$4f$ unresolved transition array (UTA) was fully evolved, with the lines from the lower ion stages still present. In fact, when the intensities of the Xe^{6+} to Xe^{9+} lines relative to the Xe^{8+} $4d$-$4f$ $^1S_0$-$^1P_1$ line were tracked from the beam energy of 180 eV through to 500 eV we found little or no change, suggesting that these charge distributions were not a strong function of beam energy under our experimental conditions. These relative intensities are listed in Table I for the electron beam energy of 180 eV. The line list presented in Table I confirms our wavelength calibration and highlights the general agreement between the calculated and observed wavelength values. A spectrum at 600 eV beam energy was acquired at a gas injection pressure of 6.7×10^{-3} Pa and electron beam current of 1.7 mA. The features of the spectrum are very similar to those of the 500 eV spectrum with

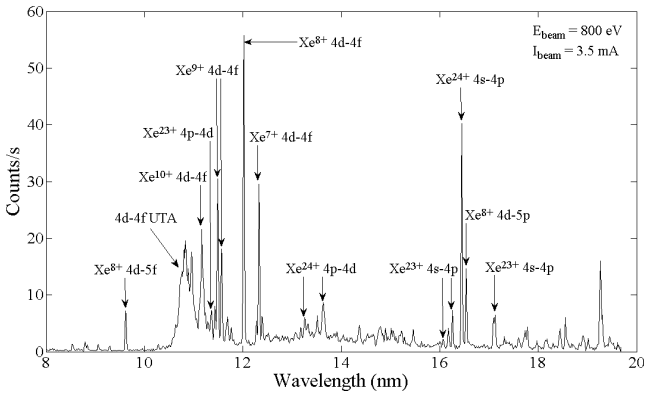

FIG. 4. The spectrum obtained at an electron beam energy of 800 eV and a gas injection pressure of 6.4×10^{-3} Pa. The highest ion stage attainable at this energy is Xe^{24+}. The $4s^2$-$4s4p$ $^1S_0$-$^1P_1$ line of Xe^{24+} [28] is observed at 16.45 nm. Also present are Xe^{24+} $4p$-$4d$ lines. The strongest feature in the spectrum is the Xe^{8+} $4d^{10}$-$4d^9 4f$ $^1S_0$-$^1P_1$ transition at 12.02 nm [4].

Xe^{20+} being the maximum charge state attainable at this energy. Biedermann *et al.* [18] measured lines of mostly weak to moderate strength from ions Xe^{17+} to Xe^{20+} between 10.6 nm and 11.2 nm, using electron beam energies ranging from 434.2 eV (for the Xe^{17+} spectrum) up to 615.9 eV (for the Xe^{20+} spectrum). These Xe^{17+} to Xe^{20+} lines coincide with the strong $4d$-$4f$ emission from the Xe^{10+} to Xe^{17+} ions observed in our spectra between 10.6 and 11.2 nm and were therefore not observable in this work. The presence of this intense $4d$-$4f$ structure in our spectra, not observed by Biedermann *et al.* [18], is most likely due to differing gas pressures employed in the two experiments (see Sec. IV D).

B. 800 eV line spectrum

Figure 4 shows the spectrum acquired at an electron beam energy of 800 eV and a gas injection pressure of 6.4×10^{-3} Pa. The maximum charge state attainable at this energy is Xe^{24+}, the energy required to produce this ion being 736 eV. When this spectrum was overlaid with the 600 eV spectrum we found seven features not common to both. The well known Xe^{24+} $4s^2$-$4s4p$ $^1S_0$-$^1P_1$ line [28] appeared very strongly at 16.45 nm in our 800 eV spectrum, the only Xe^{24+} transition to the ground state predicted to radiate in the 4 to 20 nm wavelength range. This line was also observed to be very strong by Biedermann *et al.* [18] in their study. A total of four lines from the $4p$-$4d$ and $4s$-$4p$ transitions of the Xe^{23+} ion were observed in our study. These lines appeared as moderate to very strong intensity in the spectrum of Biedermann *et al.* [18] at a beam energy of 700 eV. Biedermann *et al.* [18] also observed $4s$-$4p$ and $4p$-$4d$ lines from Xe^{22+} and Xe^{21+} using beam energies of 650 and 616 eV, respectively. These lines appeared as very weak to moderate intensity in their spectra and were predicted by our calculations but not observed in our work at all. Two additional features, not observed by Biedermann *et al.* [18] are present in our 800 eV spectrum at 13.26 and 13.63 nm. Our Cowan calculations predict the $4s^2 4p$ $^2P_{3/2}$-$4s^2 4d$ $^2D_{3/2}$ line at 13.36 nm in Xe^{23+} and the $4s^2 4p^2$ $^3P_2$-$4s^2 4p 4d$ $^1D_2$ line at 13.66 nm in Xe^{22+}. Hacker *et al.* [29] have observed two strong lines from Xe^{24+}, arising from transitions ($4p$-$4d$) not to the ground state ($4s^2$), that coincide with our measurements. Since our spectra contain none of the Xe^{22+} features observed by Biedermann *et al.* [18], and we know (because of the strong Xe^{24+} $4s^2$-$4s4p$ $^1S_0$-$^1P_1$ line) that a significant amount of Xe^{24+} is present in our trap at 800 eV, we attribute the 13.66 nm line to the $4p$-$4d$ line of Xe^{24+}. Also, since the 13.26 nm line was not observed by Biedermann *et al.* [18], this line was deemed to be the other intense Xe^{24+} $4p$-$4d$ line observed by Hacker *et al.* [29]. The wavelengths of 13.265 and 13.625 nm quoted by Hacker *et al.* [29], match our observations exactly. The observed lines of Xe^{23+} and Xe^{24+} from the 800 eV spectrum are listed in Table II.

TABLE II. Theoretical and experimental spectral lines of Xe^{23+} and Xe^{24+} observed at the NIST EBIT at an electron beam energy of 800 eV. The most intense line is Xe^{8+} $4d^{10}$-$4d^9 4f$ $^1S_0$-$^1P_1$ [4] with the Xe^{23+} and Xe^{24+} line intensities listed relative to this line in column 5.

Ion	Lower level	Upper level	NIST EBIT λ[b] (nm)	NIST EBIT Rel. Int.	Cowan[a] λ (nm)	Cowan[a] gA (10^{10} s^{-1})	Reported λ (nm)
Xe^{23+}	$4s^2 4p$ $^2P_{1/2}$	$4s^2 4d$ $^2D_{3/2}$	11.36	0.13	11.29	102	11.359[c]
Xe^{24+}	$4s4p$ $^3P_2$	$4s4d$ $^3D_3$	13.26[d]	0.11	13.18	105	13.265[e]
Xe^{24+}	$4s4p$ $^1P_1$	$4s4d$ $^1D_2$	13.63[d]	0.16	14.19	58	13.625[e]
Xe^{23+}	$4s^2 4p$ $^2P_{3/2}$	$4s4p^2$ $^2P_{3/2}$	16.07	0.04	16.04	61	16.050[c]
Xe^{23+}	$4s^2 4p$ $^2P_{1/2}$	$4s4p^2$ $^2P_{1/2}$	16.26	0.13	16.28	26	16.247[c]
Xe^{24+}	$4s^2$ $^1S_0$	$4s4p$ $^1P_1$	16.45	0.72	16.62	32	16.4412[f]
Xe^{23+}	$4s^2 4p$ $^2P_{1/2}$	$4s4p^2$ $^2D_{3/2}$	17.12	0.13	17.27	17	17.109[c]

[a]Scaling factors of F^k, G^k, R^k=90% and ζ=99% were used in the calculations.
[b]The estimated uncertainty of the wavelengths measured at NIST in this table is ±0.02 nm.
[c]Biedermann *et al.* [18].
[d]Lines are blended with Xe^{10+} $4d$-$5p$ features between 13 and 14 nm.
[e]Hacker *et al.* [29].
[f]Kaufman *et al.* [28].

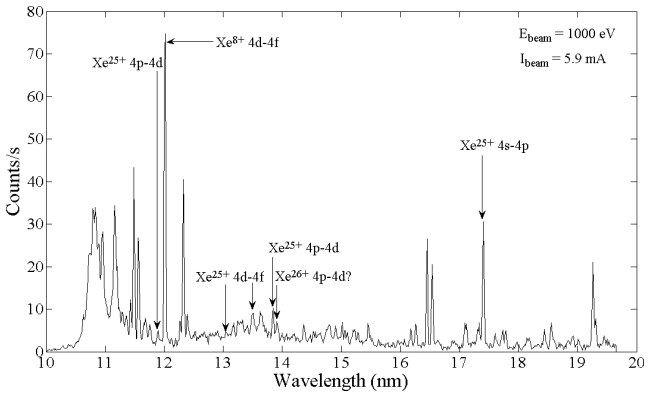

FIG. 5. The spectrum obtained at an electron beam energy of 1 keV and a gas injection pressure of 6.5×10^{-3} Pa. The highest ion stage attainable at this energy is Xe^{26+}. The Xe^{25+} $4s$-$4p$ $^2S_{1/2}$-$^2P_{3/2}$ line [28] is observed at 17.41 nm. This is the only Xe^{25+} transition to the ground state predicted to fall in the wavelength range studied in this work, while no Xe^{26+} transitions to the ground state are predicted to occur in the same range. Weak Xe^{25+} $4p$-$4d$ and $4d$-$4f$ lines are observed, the strongest of which is labeled in the above figure. The strongest feature in the spectrum is the Xe^{8+} $4d^{10}$-$4d^9 4f$ $^1S_0$-$^1P_1$ transition at 12.02 nm [4].

C. 1 keV line spectrum

Figure 5 shows the spectrum acquired at an electron beam energy of 1 keV and a gas injection pressure of 6.5×10^{-3} Pa. The maximum charge state attainable at this energy is the closed outer $3d$ shell arrangement of Xe^{26+}, the energy required to produce this ion being 856 eV. After overlaying the 1 keV spectrum with that obtained at 800 eV, six prominent features not present in the lower energy spectrum were found. The well known Xe^{25+} $3d^{10}4s$-$4p$ $^2S_{1/2}$-$^2P_{3/2}$ line [28] appeared strongly at 17.41 nm in our spectrum. This is the only Xe^{25+} transition to the ground state predicted to radiate in the 4 to 20 nm wavelength range. This line was also observed to be very strong by Biedermann *et al.* [18] in their study. No transitions to the ground state of the Xe^{26+} ion are predicted to radiate in this wavelength range. In the absence of any alternative line candidates with transitions to the ground state, a total of four lines from the $4p$-$4d$ and $4d$-$4f$ transitions of the Xe^{25+} ion were identified in our study. These lines have been previously observed by Kaufman *et al.* [28]. The Xe^{25+} lines observed in the 1 keV spectrum are listed in Table III. Also listed in Table III is a line which we observed at 13.91 nm with a relative intensity of 0.09. We calculated the $3d^9 4p$-$3d^9 4d$ $^3F_4$-$^3G_5$ and $3d^9 4d$-$3d^9 4f$ $^1D_2$-$^1D_2$ transitions in Xe^{26+} to be at 13.89 nm and 13.86 nm, respectively. We tentatively attribute this line to the $3d^9 4p$-$3d^9 4d$ transition since it has a calculated wavelength which is in better agreement with the observed value and it also has a calculated gA value of 1.3×10^{12} s^{-1} compared to 1.1×10^{11} s^{-1} for the $3d^9 4d$-$3d^9 4f$ transition.

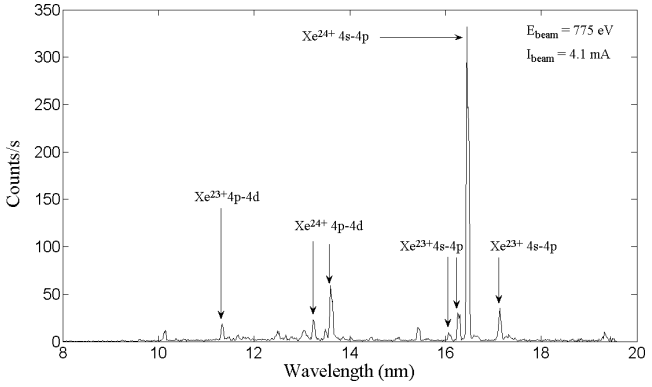

FIG. 6. The spectrum obtained at an electron beam energy of 775 eV and a gas injection pressure of 9.1×10^{-6} Pa. The highest ion stage attainable at this energy is Xe^{24+}. The spectrum is dominated by emission from the Xe^{24+} and Xe^{23+} ions. The $4s^2$-$4s4p$ $^1S_0$-$^1P_1$ line of Xe^{24+} at 16.45 nm [28] is the strongest observed feature in the spectrum. The corresponding wavelengths and transitions are listed in Table II.

D. Effect of gas injection pressure

The spectrum of Fig. 6 was obtained with an electron beam energy of 775 eV and a gas injection pressure of 9.1

TABLE III. Theoretical and experimental spectral lines of Xe^{25+} and Xe^{26+} observed at the NIST EBIT at an electron beam energy of 1000 eV. The most intense line is Xe^{8+} $4d^{10}$-$4d^9 4f$ $^1S_0$-$^1P_1$ [4] with the Xe^{25+} and Xe^{26+} line intensities listed relative to this line in column 5.

Ion	Lower level	Upper level	NIST EBIT λ[b] (nm)	NIST EBIT Rel. Int.	Cowan[a] λ (nm)	Cowan[a] gA (10^{10} s^{-1})	Reported λ (nm)
Xe^{25+}	$3d^{10}4p$ $^2P_{1/2}$	$3d^{10}4d$ $^2D_{3/2}$	11.90	0.07	11.91	66	11.8935[c]
Xe^{25+}	$3d^{10}4d$ $^2D_{3/2}$	$3d^{10}4f$ $^2F_{5/2}$	13.04[d]	0.06	13.06	79	13.0428[c]
Xe^{25+}	$3d^{10}4d$ $^2D_{5/2}$	$3d^{10}4f$ $^2F_{7/2}$	13.51[d]	0.12	13.47	103	13.4852[c]
Xe^{25+}	$3d^{10}4p$ $^2P_{3/2}$	$3d^{10}4d$ $^2D_{5/2}$	13.84[d]	0.14	13.80	77	13.8389[c]
Xe^{25+}	$3d^{10}4s$ $^2S_{1/2}$	$3d^{10}4p$ $^2P_{3/2}$	17.41	0.41	17.46	20	17.3938[c]
Xe^{26+}	$3d^9 4p$ $^3F_4$	$3d^9 4d$ $^3G_5$[e]	13.91	0.09	13.89	132	

[a]Scaling factors of F^k, G^k, R^k=90% and ζ=99% were used in the calculations.
[b]The estimated uncertainty of the wavelengths measured at NIST in this table is ±0.02 nm.
[c]Kaufman *et al.* [28].
[d]Line blended with Xe^{10+} $4d$-$5p$ features between 13 and 14 nm.
[e]Tentative assignment.

$\times 10^{-6}$ Pa. The highest ion stage attainable at this energy is Xe^{24+}. This spectrum can be compared to that shown in Fig. 4, obtained at an electron beam energy of 800 eV but at the much higher gas injection pressure of 6.4×10^{-3} Pa. The effect of decreasing the gas injection pressure on the observed spectrum is immediately noticeable. The features of the higher pressure spectrum emanating from ion stages Xe^{6+} to Xe^{10+}, along with the $4d$-$4f$ features of the Xe^{11+} to Xe^{17+} UTA, are completely absent at the lower pressure. Instead, the lower pressure spectrum is dominated by lines arising from Xe^{24+} and Xe^{23+} ions. This reflects a change in the equilibrium charge balance in the EBIT with changing gas pressure, due mainly to the rate of charge exchange becoming much less at reduced pressures. The seven prominent features of the lower pressure spectrum arising from the Xe^{23+} and Xe^{24+} ions and labeled in Fig. 6, are those same lines identified in the higher pressure spectrum of Fig. 4 and listed in Table II. The line intensities at the different gas pressures can also be compared by looking at Fig. 4 and Fig. 6. The $4s^2$-$4s4p$ $^1S_0$-$^1P_1$ line of Xe^{24+} at 16.45 nm is at least 10 times stronger at the lower pressure. The intensity ratio of the $4s$-$4p$ line of Xe^{24+} to the $4s$-$4p$ isolated lines of Xe^{23+} is about 7 at the higher pressure compared to approximately 10 at the lower pressure. This is attributed to a 40% increase in the number density of Xe^{24+} ions relative to Xe^{23+} as the pressure is reduced. Therefore, the effect of lowering the neutral gas injection pressure is to suppress the lower charge state ions present in the trap and shift the ion population toward the maximum energetically allowed by the electron beam.

E. 2 to 8 keV line spectra

The spectra listed in this section were acquired using a gas injection pressure of 6.7×10^{-3} Pa. By tuning the electron beam energy from 2 up to 8 keV, ion stages up to a maximum of Xe^{46+} can be created in the trap. Calculations predict that the spectra obtained in this beam energy window should be largely dominated by $3p$-$3d$ transitions in the ion stages Xe^{27+} to Xe^{41+} with the strongest emission occurring between 4 and 7 nm. The $3p$-$3d$ emission predicted to occur between 4 and 4.5 nm was not visible in our data due to the reduced sensitivity of our spectrometer in this region. Figure 7 shows the predicted emission from the $3p$-$3d$ transition array, between 4.5 and 7 nm, for ion stages Xe^{27+} to Xe^{34+}. This $3p$-$3d$ emission is fused into a narrow band near 5 nm and shifts to longer wavelengths with increasing ionization. Spectra obtained for electron beam energies between 2 and 4 keV contain a large number of low intensity features arising from these transitions. Due to the large number of lines and their low intensities, coupled with the large spread of charge states present in the trap, the assignment of a given feature to a particular ion was not accomplished for these ion stages in this work. Figure 8 shows simulated spectra, based on the predictions of the Cowan code, for the ion stages Xe^{35+} up to Xe^{43+}. The spectra of these ion stages are predicted to contain fewer features than the spectra of the preceding eight ion stages. Consequently we found that at electron beam energies above 4 keV the spectra were greatly simplified, compared to those spectra obtained between 2 and 4 keV.

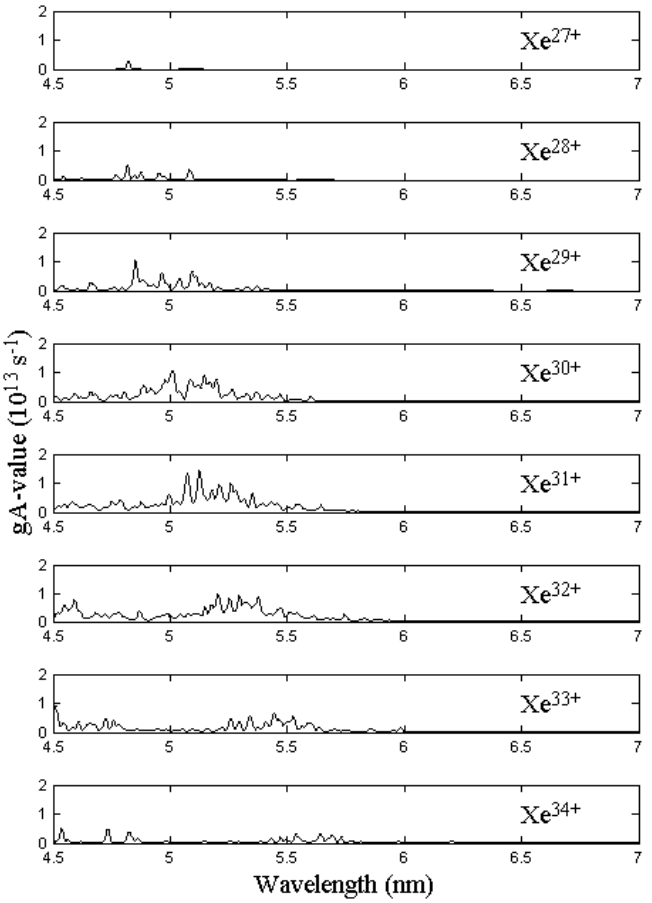

FIG. 7. Simulated spectra based on the predictions of the Cowan code for $3p$-$3d$ transitions in eight charge states of xenon. Each of the predicted lines was convolved with a Gaussian function of 0.02 nm width.

The spectra obtained between beam energies of 6 and 8 keV were very similar and contained the least number of features and we sought first to identify these. Figure 9 shows the 4.5 to 7 nm wavelength region of the spectrum taken at a beam energy of 8 keV. Figure 10 shows the same spectrum over the full wavelength range of 4.5 to 20 nm, with the uncertainty in the wavelength scale estimated to be 0.003 nm. We identified the Xe^{42+} $3s^2$-$3s3p$ $^1S_0$-$^1P_1$ and the Xe^{43+} $2p^63s$-$2p^63p$ $^2S_{1/2}$-$^2P_{3/2}$ lines at 6.288 and 6.657 nm, respectively, observed previously in the spectra obtained from EBIT by Träbert *et al.* [17] at 6.2875 ± 0.0012 nm and 6.6574 ± 0.0020 nm. Seely *et al.* [30] measured a wavelength of 6.658 ± 0.003 nm for the Xe^{43+} $2p^63s$-$2p^63p$ $^2S_{1/2}$-$^2P_{3/2}$ line based on laser plasma observations. We confirmed the presence of the Xe^{42+} and Xe^{43+} ions in the trap by observing two additional lines from these ions in our spectra. Our calculations predict the $2p^63s$-$2p^63p$ $^2S_{1/2}$-$^2P_{1/2}$ transition in Xe^{43+} to emit at a wavelength of 12.38 nm. Reader *et al.* [31] extrapolated their data for lower ion stages to obtain least-squares-fitted wavelengths for the Xe^{43+} ion and they predicted a wavelength value of 12.3897 nm for this transition.

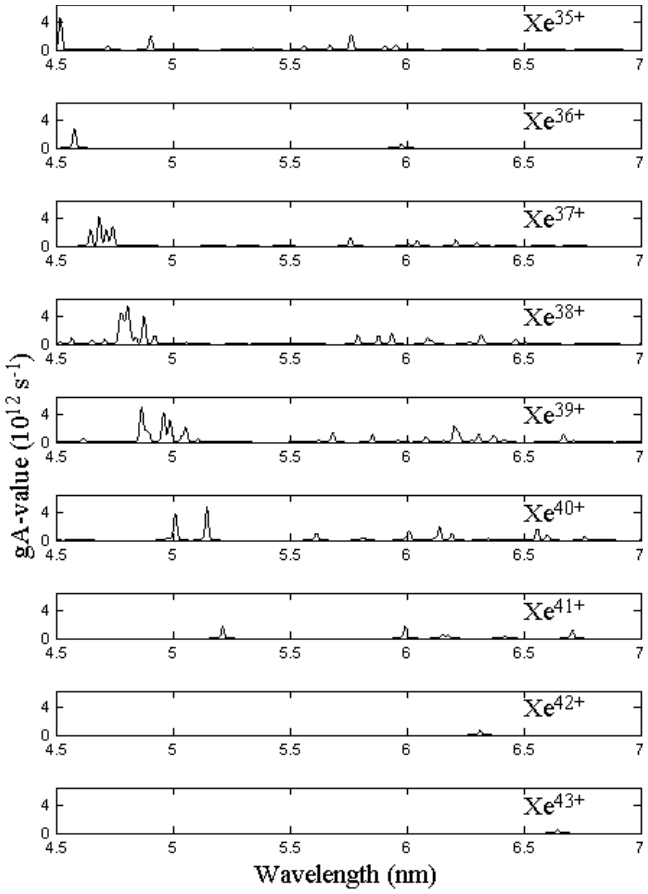

FIG. 8. Simulated spectra based on the predictions of the Cowan code for $3p$-$3d$ and $3s$-$3p$ transitions in nine charge states of xenon. Each of the predicted lines was convolved with a Gaussian function of 0.02 nm width.

We observed this line at 12.395 nm in our spectrum. We also calculated a wavelength of 13.35 nm corresponding to the $3s^2$-$3s3p$ $^1S_0$-$^3P_1$ transition in Xe^{42+}. This line was previously measured at 12.993±0.003 nm by Seely *et al.* [32]

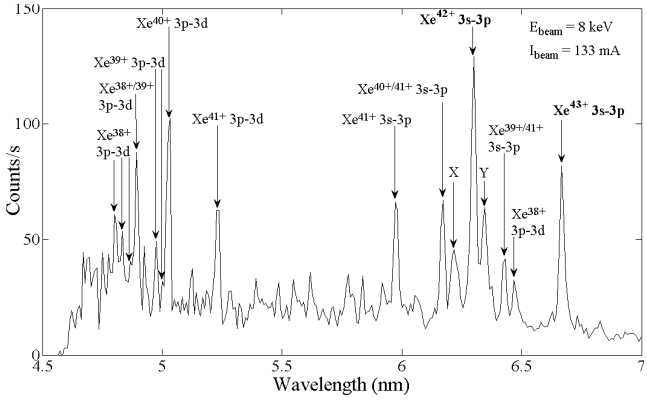

FIG. 9. A section of the spectrum obtained at an electron beam energy of 8 keV and a gas injection pressure of 6.7×10^{-3} Pa. The highest ion stage observed at this energy was Xe^{43+}. The features labeled *X* and *Y* are the broad features observed at 6.207 and 6.333 nm, respectively. A number of lines are predicted to contribute to these structures and these are listed in Table IV.

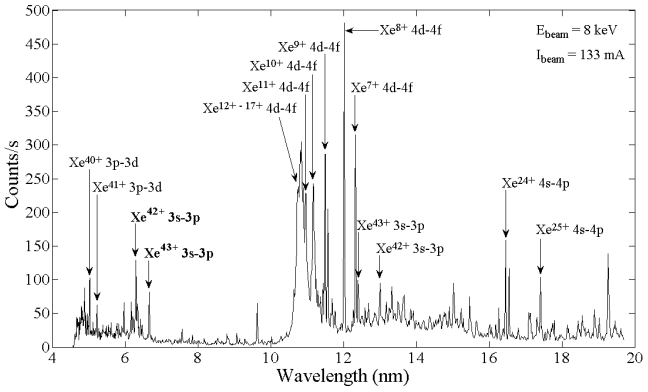

FIG. 10. The full spectrum obtained at an electron beam energy of 8 keV and a gas injection pressure of 6.7×10^{-3} Pa. Emission is observed from a wide range of charge states, from Xe^{6+} to Xe^{43+}. The strongest feature in the spectrum is the Xe^{8+} $4d^{10}$-$4d^9 4f$ $^1S_0$-$^1P_1$ transition at 12.02 nm [4].

using a tokamak as their source. In addition, Ekberg *et al.* [33] fitted the difference between observed and calculated level energies in the magnesium-like ions of Mo, Rh, Ag, Cd, In, Sn, Sb, I, and Cs and interpolated these values to derive a fitted wavelength of 12.9916 nm for this Xe^{42+} $3s$-$3p$ $^1S_0$-$^3P_1$ transition. This line was observed at a wavelength of 12.999 nm in our work. Reader *et al.* [31] also published fitted wavelengths corresponding to $3p$-$3d$ and $3d$-$4f$ transitions in the Xe^{43+} ion. These transitions are not to the ground state of the emitting ion and were not observed in this work. Consequently, all of the new assignments of the 8 keV spectrum presented here involve transitions to the ground state of the emitting ion.

Table IV lists eighteen prominent features observed in the measured spectrum at 8 keV, arising from the ion stages Xe^{37+} through to Xe^{43+}. The Xe^{40+} and Xe^{41+} $3p$-$3d$ lines, identified by Träbert *et al.* [17] from the calculations of Huang [34,35], were observed in this work at 5.007 and 5.213 nm, respectively. Our calculated wavelengths for these lines lie within 0.02 nm of those values predicted by Huang [34,35]. Träbert *et al.* [17] did not assign experimental wavelength values to these features. In most cases two or more lines were calculated with wavelengths that closely matched the observed wavelength. In these cases all of the strong calculated transitions were tabulated. For example, three strong Xe^{39+} $3p^3$-$3p^2 3d$ lines and a strong Xe^{38+} $3p^4$-$3p^3 3d$ line were calculated with wavelengths between 4.87 and 4.88 nm. As these lines coincide with the measured feature at 4.873 nm, this observed feature may contain a blend of the Xe^{38+} and Xe^{39+} calculated lines and the associated transitions are listed in Table IV. The features observed at 6.207 and 6.333 nm appear quite broad in the measured spectrum and these are likely to contain a mix of the corresponding calculated lines listed in Table IV. However, analysis suggests that the 6.207 nm feature may be predominantly due to the Xe^{37+} $3p^5$-$3p^4 3d$ $^2P_{3/2}$-$^4F_{5/2}$ transition since the observed feature was present more strongly at an electron beam energy of 3 keV, and seemed to gradually weaken as the beam energy was increased towards 8 keV. This seems to indicate that the observed feature is due to a lower ion stage than the

TABLE IV. Theoretical and experimental spectral lines of Xe^{37+} to Xe^{43+} observed at the NIST EBIT at an electron beam energy of 8 keV. The most intense line is Xe^{8+} $4d^{10}$-$4d^9 4f$ $^1S_0$-$^1P_1$ [4], with line intensities listed relative to this line in column 5.

Ion	Lower level	Upper level	NIST EBIT λ[b] (nm)	NIST EBIT Rel. Int.	Cowan[a] λ (nm)	Cowan[a] gA (10^{10} s^{-1})	Reported λ (nm)
Xe^{38+}	$3s^2 3p^4\ ^3P_2$	$3p^3 3d\ ^3P_2$	4.783[c]	0.13	4.77	420	
Xe^{38+}	$3s^2 3p^4\ ^3P_2$	$3p^3 3d\ ^3D_3$	4.813[c]	0.11	4.81	513	
Xe^{38+}	$3s^2 3p^4\ ^1D_2$	$3p^3 3d\ ^1D_2$	4.846[d]	0.08	4.84	116	
Xe^{39+}	$3s^2 3p^3\ ^2P_{3/2}$	$3p^2 3d\ ^4P_{3/2}$	4.873	0.25	4.87	378	
Xe^{39+}	$3s^2 3p^3\ ^4S_{3/2}$	$3p^2 3d\ ^2D_{3/2}$			4.87	204	
Xe^{39+}	$3s^2 3p^3\ ^4S_{3/2}$	$3p^2 3d\ ^2D_{5/2}$			4.88	134	
Xe^{38+}	$3s^2 3p^4\ ^1D_2$	$3p^3 3d\ ^1F_3$			4.88	488	
Xe^{39+}	$3s^2 3p^3\ ^2P_{3/2}$	$3p^2 3d\ ^4P_{5/2}$	4.955	0.10	4.96	338	
Xe^{39+}	$3s^2 3p^3\ ^2P_{1/2}$	$3p^2 3d\ ^2D_{3/2}$			4.96	236	
Xe^{39+}	$3s^2 3p^3\ ^2D_{5/2}$	$3p^2 3d\ ^2F_{7/2}$	4.980[e]	0.07	4.99	384	
Xe^{40+}	$3s^2 3p^2\ ^3P_0$	$3p3d\ ^3D_1$	5.007	0.33	5.01	209	
Xe^{40+}	$3s^2 3p^2\ ^3P_1$	$3p3d\ ^3D_2$			5.01	122	
Xe^{40+}	$3s^2 3p^2\ ^3P_1$	$3p3d\ ^3P_1$			5.01	160	
Xe^{41+}	$3s^2 3p\ ^2P_{1/2}$	$3s^2 3d\ ^2D_{3/2}$	5.213	0.23	5.21	204	
Xe^{41+}	$3s^2 3p\ ^2P_{3/2}$	$3s3p^2\ ^2P_{3/2}$	5.963	0.15	5.99	221	
Xe^{40+}	$3s^2 3p^2\ ^3P_2$	$3s3p^3\ ^3P_2$	6.158	0.20	6.14	225	
Xe^{41+}	$3s^2 3p\ ^2P_{1/2}$	$3s3p^2\ ^2P_{1/2}$			6.16	75	
Xe^{37+}	$3s^2 3p^5\ ^2P_{3/2}$	$3p^4 3d\ ^4F_{5/2}$	6.207	0.12	6.21	108	
Xe^{39+}	$3s^2 3p^3\ ^2P_{3/2}$	$3p^2 3d\ ^2D_{5/2}$			6.20	271	
Xe^{39+}	$3s^2 3p^3\ ^2D_{5/2}$	$3s3p^4\ ^2D_{5/2}$			6.22	151	
Xe^{40+}	$3s^2 3p^2\ ^1D_2$	$3s3p^3\ ^2D_2$			6.19	120	
Xe^{41+}	$3s^2 3p\ ^2P_{3/2}$	$3s3p^2\ ^2S_{1/2}$			6.18	51	
Xe^{42+}	$3s^2\ ^1S_0$	$3s3p\ ^1P_1$	6.288	0.43	6.32	90	6.2875[f]
Xe^{38+}	$3s^2 3p^4\ ^1D_2$	$3p^3 3d\ ^1F_3$	6.333[g]	0.21	6.32	130	
Xe^{39+}	$3s^2 3p^3\ ^4S_{3/2}$	$3p^2 3d\ ^4F_{5/2}$			6.31	137	
Xe^{40+}	$3s^2 3p^2\ ^3P_0$	$3s3p^3\ ^3D_1$			6.35	27	
Xe^{41+}	$3s^2 3p^1\ ^2P_{1/2}$	$3s3p^2\ ^2D_{3/2}$	6.416	0.14	6.42	41	
Xe^{39+}	$3s^2 3p^3\ ^4S_{3/2}$	$3s3p^4\ ^4P_{3/2}$			6.42	44	
Xe^{38+}	$3s^2 3p^4\ ^3P_2$	$3p^3 3d\ ^3F_3$	6.459	0.08	6.47	91	
Xe^{43+}	$3s\ ^2S_{1/2}$	$3p\ ^2P_{3/2}$	6.657	0.22	6.65	64	6.6574[f]
Xe^{43+}	$3s\ ^2S_{1/2}$	$3p\ ^2P_{1/2}$	12.395	0.21	12.39	5	12.3897[h]
Xe^{42+}	$3s^2\ ^1S_0$	$3s3p\ ^3P_1$	12.999	0.20	13.35	2	12.993[i]

[a]Scaling factors of F^k, G^k, R^k=95% and ζ=99% were used in the calculations with the exception of the Xe^{37+} ion calculations where a value of F^k, G^k, R^k=90% was employed.
[b]The estimated uncertainty of the wavelengths measured at NIST in this table is ±0.003 nm.
[c]Calculations predict a number of lines from the Xe^{38+} ion that merge to form a $3p$-$3d$ structure unresolved in our spectra. The peak wavelengths are listed here along with the strongest predicted transitions falling within this structure.
[d]This feature is blended with the 4.873 nm line.
[e]This feature is blended with the 5.007 nm line.
[f]Träbert *et al.* [17].
[g]Broad structure.
[h]Reader *et al.* [31].
[i]Seely *et al.* [32].

alternative ion stages of Xe^{39+} to Xe^{41+}, listed in Table IV, particularly as no emission from these higher ion stages was observed in the spectrum at 3 keV.

Although ions up to Xe^{46+} (with a production threshold of 7.89 keV [27]) were energetically possible at this beam energy no emission was observed from ion stages higher than

TABLE V. Theoretical and experimental spectral lines of Xe^{35+} to Xe^{37+} observed at the NIST EBIT at an electron beam energy of 4 keV. The most intense line is Xe^{8+} $4d^{10}$-$4d^9 4f$ $^1S_0$-$^1P_1$ [4], with line intensities listed relative to this line in column 5.

Ion	Lower level	Upper level	NIST EBIT λ[b] (nm)	NIST EBIT Rel. Int.	Cowan[a] λ (nm)	Cowan[a] gA (10^{10} s^{-1})	Reported λ (nm)
Xe^{35+}	$3s^2 3d^1$ $^2D_{5/2}$	$3p^5 3d^2$ $^4F_{5/2}$	5.760	0.12	5.76	140	
Xe^{35+}	$3s^2 3d^1$ $^2D_{3/2}$	$3p^5 3d^2$ $^4F_{5/2}$			5.76	175	
Xe^{37+}	$3s^2 3p^5$ $^2P_{1/2}$	$3p^4 3d$ $^2P_{1/2}$			5.76	136	
Xe^{37+}	$3s^2 3p^5$ $^2P_{1/2}$	$3p^4 3d$ $^2D_{3/2}$	6.045	0.07	6.04	98	
Xe^{36+}	$3s^2 3p^6$ $^1S_0$	$3p^5 3d$ $^3D_1$			5.98	66	
Xe^{37+}	$3s^2 3p^5$ $^2P_{3/2}$	$3p^4 3d$ $^4P_{3/2}$	6.265	0.08	6.30	54	

[a]Scaling factors of F^k, G^k, R^k=90% and ζ=99% were used in the calculations.
[b]The estimated uncertainty of the wavelengths measured at NIST in this table is ±0.003 nm.

Xe^{43+}. According to our calculations, there are no transitions from Xe^{44+} and Xe^{45+} ions to their ground state in the observed wavelength range. However, our calculations predict three $2s^2 2p^4$-$2s2p^5$ transitions of the Xe^{46+} ion at 4.68 nm ($^3P_0$-$^3P_1$), 4.78 nm ($^3P_1$-$^3P_2$), and 5.14 nm ($^1D_2$-$^3P_2$). The absence of these lines is most likely due to the competing processes of ionization, recombination, and charge exchange that occur within the trap, resulting in insufficient Xe^{46+} ions under our trap conditions. The cross section for radiative recombination increases with ion stage and serves to drive the charge balance in the trap to lower ion stages. The reverse is true for lower ion stages, where ionization is the dominant process, resulting in observed emission immediately as the ionization threshold is exceeded. The relatively high gas injection pressures employed in this work have also contributed to this effect, with the process of charge exchange driving the charge balance in the trap to lower ion stages.

Also worth noting is the absence of the Xe^{40+} $3p^2$-$3p3d$ $^1D_2$-$^3D_2$ and $^1D_2$-$^3D_3$ lines that should be unresolved in our spectrum with the resultant feature calculated to lie at 5.14 nm. This feature is predicted to be of similar strength to the other Xe^{40+} $3p^2$-$3p3d$ feature observed strongly in our spectrum at 5.007 nm. We checked if the strong line observed at 5.213 nm, and identified as Xe^{41+} $3s^2 3p$-$3s^2 3d$ $^2P_{1/2}$-$^2D_{3/2}$, could be attributed to this Xe^{40+} $3p$-$3d$ feature by adjusting the spin-orbit integral, ζ, up to 110% of its HF value as is sometimes necessary for highly charged ion calculations where relativistic effects are important. However, this adjustment resulted in the Xe^{40+} $3p$-$3d$ feature being shifted to a shorter wavelength and further away from the observed line position. A similar effect was found in the calculation of the well known $3s$-$3p$ lines of Xe^{42+} and Xe^{43+}. It was concluded that the scaling factor of ζ=99% is optimum for these calculations and the 5.213 nm feature, calculated at 5.21 nm, is correctly attributed to the $3s^2 3p$-$3s^2 3d$ $^2P_{1/2}$-$^2D_{3/2}$ transition in the Xe^{41+} ion. The absence of the Xe^{40+} $3p$-$3d$ feature may be due to the level population mechanisms in EBIT. Table V lists three features observed in our spectrum at a beam energy of 4 keV. These lines were either absent or present only very weakly in the spectra at 8 keV. This suggests that these lines are due to ion stages lower than those contributing strongly to the 8 keV spectra. Calculations revealed six lines from the Xe^{35+} to Xe^{37+} ions that best agree with the observed wavelengths.

F. Excitation-autoionization of Xe^{41+} and Xe^{42+}

Figure 11 shows the electron beam energy dependence of the intensity of the (a) Xe^{43+} $2p^6 3s$-$3p$ $^2S_{1/2}$-$^2P_{3/2}$ and (b) Xe^{42+} $3s^2$-$3s3p$ $^1S_0$-$^1P_1$ measured lines. These lines are labeled in bold in Figs. 9 and 10. Considering the Xe^{43+} line plotted in Fig. 11(a), this line is not present in the measured spectrum, within the one-sigma noise level, below a beam energy of about 3.9 keV, although the production threshold for this ion is 3.24 keV. Above 3.9 keV, the line intensity rises gradually towards a beam energy of about 4.5 keV, above which an abrupt increase in line intensity is observed towards about 5 keV. The absence of the Xe^{43+} line as its production threshold was exceeded, and up to an energy of 3.9 keV, is attributed to the process of charge exchange, pro-

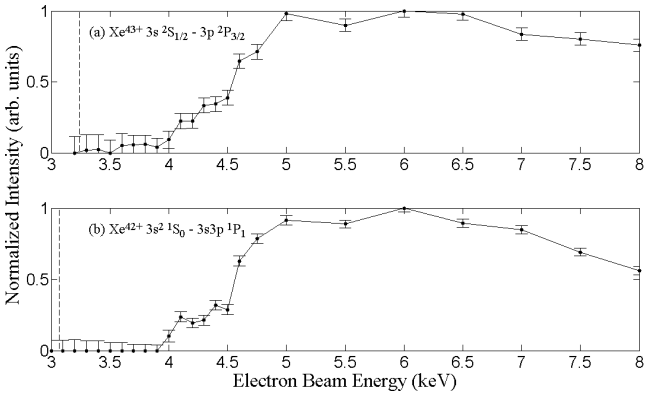

FIG. 11. (a) Electron beam energy dependence of the intensity of the Xe^{43+} $2p^6 3s$-$2p^6 3p$ $^2S_{1/2}$-$^2P_{3/2}$ line, measured at 6.657 nm. (b) Electron beam energy dependence of the intensity of the Xe^{42+} $3s^2$-$3s3p$ $^1S_0$-$^1P_1$ line, measured at 6.288 nm. These lines are labeled in bold in Figs. 9 and 10. The data are normalized to the electron beam current. The vertical lines represent the energy threshold for production of the charge states Xe^{42+} (3.07 keV) and Xe^{43+} (3.24 keV). The change in slope near 4.5 keV (~4.3 keV after space charge correction) is attributed to the onset of $2p$-$3l$ excitation autoionization. Error bars are at the one-sigma level.

ceeding at a much faster rate than the ionization of the preceding ion stage, at these energies, for the neutral gas densities employed in these experiments. This leads to the rapid quenching of the Xe^{43+} ion for these energies. The ionization rate of Xe^{42+} (EI_{42+}), peaking at about a factor of 2.5 above the threshold energy, begins to exceed the charge exchange rate of Xe^{43+} (CX_{43+}) as the energy is increased above about 3.9 keV, resulting in observed emission from the Xe^{43+} ion. Calculations of EI_{42+} and CX_{43+} were found to predict this behavior, with the shape of the net rate (EI_{42+}-CX_{43+}) curve matching that of the observed intensity curve, between 3.9 and 4.5 keV. The absence of threshold behavior for this ion is contrary to what was observed at lower energies, where, for example, emission from the Xe^{11+} ion was observed immediately as its production threshold was exceeded (Sec. IV A, Fig. 3).

The abrupt increase in slope at about 4.5 keV is attributed to the enhancement of the total ionization cross section by excitation autoionization of $2p$ electrons to the $n=3$ shell in Xe^{42+}. These measurements are consistent with calculated electron-impact ionization cross sections for Xe^{43+} into Xe^{44+} by Reed *et al.* [36], and subsequent EBIT measurements of the same ion by Schneider *et al.* [37]. These studies have shown that for beam energies above 4.3 keV it is possible to excite $2p$ electrons to the $n=3$ levels and produce autoionizing states of the Xe^{43+} ion. It was shown [36,37] that near the thresholds for these excitations the ionization cross section increases abruptly (by a factor of about 4, between 4 and 5 keV) due to the excitation-autoionization contributions to the total ionization cross section. Howald *et al.* [38] measured absolute electron-impact ionization cross sections in low-Z Mg-like ions and found that the relative magnitude of the indirect ionization process increases dramatically in comparison with the direct process along the isoelectronic sequence.

A similar intensity profile to Fig. 11(a) was observed in Fig. 11(b) for the Xe^{42+} $3s^2$-$3s3p$ $^1S_0$-$^1P_1$ line, measured at 6.288 nm, revealing both direct and indirect contributions to the total ionization cross section in Xe^{41+}.

The data of Fig. 11 is shown normalized to the electron beam current. Similar profiles were observed when the Xe^{42+} and Xe^{43+} line intensities were plotted relative to the strong Xe^{8+} $4d^{10}$-$4d^9 4f$ $^1S_0$-$^1P_1$ line at 12.02 nm. It should also be noted that the energy scale of Fig. 11 is not corrected for space charge defects in the electron beam. For a 4.5 keV, 108 mA electron beam, this correction is estimated to be ~−250 eV. This is an upper bound as it does not include the positive space charge of the trapped ions. When this correction is applied to the beam energy in Fig. 11, the sharp increase in line intensity occurs at ~4.3 keV, for both curves, consistent with the excitation of a $2p$ electron to the $n=3$ shell. While Reed *et al.* [36] predict the ionization cross section to increase in a series of abrupt steps corresponding to the $n=2$ electron excitations, the energy resolution of Fig. 11 is not sufficient to show this step structure in detail. However, the data for both Xe^{43+} and Xe^{42+} is consistent with the enhancement of the ionization cross section by excitation autoionization, in the Xe^{42+} and Xe^{41+} ions.

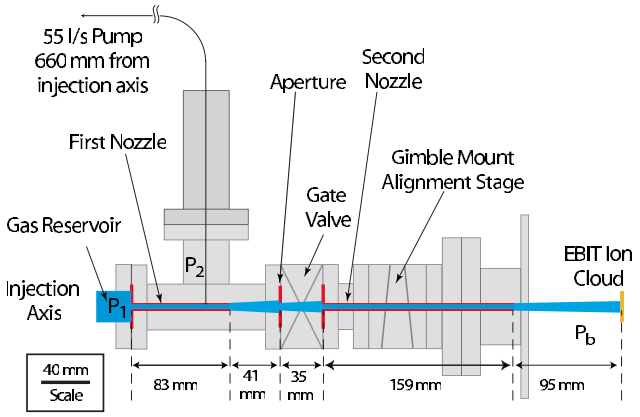

FIG. 12. (Color online) Details of the EBIT gas injector setup. $P1$ is the gas injector reservoir pressure, with $P2$ typically two orders of magnitude smaller than this. Pb is the pressure measured outside of the trap region ($<10^{-9}$ Pa). Note that the actual background pressure inside the trap region will be less than Pb, due to cryopumping by the surrounding 4.2 K surfaces.

V. SUMMARY AND CONCLUSIONS

We have presented spectra of xenon in the 4.5 to 20 nm wavelength range, obtained from xenon ions trapped in an EBIT. With the EBIT's capability to selectively produce and excite particular ion stages, we could observe the radiation from a wide range of charge states. The present study has led to the identification of lines corresponding to transitions within the ions of Xe^{6+} up to Xe^{43+}. We have performed atomic structure calculations using the Cowan suite of codes and found that our calculations could deliver results within 0.07 nm of the accepted wavelengths in the majority of cases. Ion stages Xe^{27+} through to Xe^{34+} have been shown to produce complex spectra corresponding to $3p$-$3d$ transitions where the emission is fused into a narrow band near 5 nm and shifts to longer wavelengths with increasing ionization. Due to the complexity of the $3p$-$3d$ emission arising from these ion stages we did not seek to identify these features in our spectra. Instead, we sought to make assignments based on the emission from Xe^{35+} through to Xe^{46+} since these ions have a lower density of emitting features that do not overlap in energy and therefore could be resolved in our spectra. The calculations were used to identify seventeen new features corresponding to $3s$-$3p$ and $3p$-$3d$ transitions in the ion stages Xe^{35+} through Xe^{41+}. We found that our spectra contained a density of features greater than normally associated with EBIT spectra and often contained lines from a very wide range of charge states up to the maximum energetically allowed, at the electron beam energy. We presented a spectrum acquired at a beam energy of 800 eV that contained features from Xe^{6+} through to Xe^{24+}, and we showed that by reducing the gas injection pressure by approximately two orders of magnitude a spectrum dominated by radiation from the highest two energetically allowed ion stages could be obtained. We also observed the enhancement of the ionization cross sections of Xe^{41+} and Xe^{42+}, by excitation-autoionization of $n=2$ electrons to $n=3$ levels, by tracking

the energy dependence of the intensities of spectral lines arising from the resulting Xe^{42+} and Xe^{43+} charge states. The line intensities were seen to increase sharply as the $n=2$ excitation threshold was exceeded, consistent with an abrupt increase in the total ionization cross section at these energies. The suppression of the Xe^{42+} and Xe^{43+} ions as their production thresholds were exceeded, due to the dominant process of charge exchange under certain EBIT operating conditions, was also observed.

ACKNOWLEDGMENTS

This work was supported in part by Science Foundation Ireland under Investigator Grant 02/IN.1/I99 and International SEMATECH under LITH152.

APPENDIX: GAS INJECTOR SETUP

Details of the EBIT gas injector setup are shown in Fig. 12.

[1] S. S. Churilov and Y. N. Joshi, Phys. Scr. **65**, 35 (2002).
[2] V. Kaufman and J. Sugar, J. Opt. Soc. Am. B **4**, 1919 (1987).
[3] V. Kaufman and J. Sugar, J. Opt. Soc. Am. B **1**, 38 (1984).
[4] S. S. Churilov and Y. N. Joshi, Phys. Scr. **65**, 40 (2002).
[5] S. S. Churilov, Y. N. Joshi, J. Reader, and R. R. Kildiyarova, Phys. Scr. **70**, 26 (2004).
[6] G. O'Sullivan, J. Phys. B **15**, L765 (1982).
[7] W. Svendsen and G. O'Sullivan, Phys. Rev. A **50**, 3710 (1994).
[8] G. Schriever, K. Bergmann, and R. Lebert, J. Vac. Sci. Technol. B **17**, 2058 (1999).
[9] M. A. Klosner and W. T. Silvast, J. Opt. Soc. Am. B **17**, 1279 (2000).
[10] *EUV Sources for Lithography*, edited by V. Bakshi (SPIE Press, Bellingham, WA, 2006).
[11] P. Mandelbaum, M. Finkenthal, J. L. Schwob, and M. Klapisch, Phys. Rev. A **35**, 5051 (1987).
[12] J. Bauche, C. Bauche-Arnoult, M. Klapisch, P. Mandelbaum, and J. L. Schwob, J. Phys. B **20**, 1443 (1987).
[13] C. Bauche-Arnoult and J. Bauche, Phys. Scr., T **T40**, 58 (1992).
[14] G. O'Sullivan and P. K. Carroll, J. Opt. Soc. Am. **71**, 227 (1981).
[15] P. K. Carroll and G. O'Sullivan, Phys. Rev. A **25**, 275 (1982).
[16] K. Fahy *et al.*, J. Phys. D **37**, 3225 (2004).
[17] E. Träbert, P. Beiersdorfer, J. K. Lepson, and H. Chen, Phys. Rev. A **68**, 042501 (2003).
[18] C. Biedermann, R. Radkte, G. Fuβmann, J. L. Schwob, and P. Mandelbaum, Nucl. Instrum. Methods Phys. Res. B **235**, 126 (2005).
[19] A. Bar-Shalom, M. Klapisch, and J. Oreg, J. Quant. Spectrosc. Radiat. Transf. **71**, 169 (2001).
[20] J. D. Gillaspy, Phys. Scr., T **T71**, 99 (1997).
[21] B. Blagojević *et al.*, Rev. Sci. Instrum. **76**, 083102 (2005).
[22] T. Kita, T. Harada, N. Nakano, and H. Kuroda, Appl. Opt. **22**, 512 (1983).
[23] D. W. Savin, P. Beiersdorfer, S. M. Kahn, B. R. Beck, G. V. Brown, M. F. Gu, D. A. Liedahl, and J. H. Scofield, Rev. Sci. Instrum. **71**, 3362 (2000).
[24] R. D. Cowan, *The Theory of Atomic Structure and Spectra* (University of California Press, Berkeley, CA, 1981).
[25] C. A. Morgan, F. G. Serpa, E. Takács, E. S. Meyer, J. D. Gillaspy, J. Sugar, J. R. Roberts, C. M. Brown, and U. Feldman, Phys. Rev. Lett. **74**, 1716 (1995).
[26] J. F. Wyart, C. Bauche-Arnoult, E. Luc-Koenig, and T. Group, Phys. Scr. **32**, 103 (1985).
[27] G. C. Rodrigues, P. Indelicato, J. P. Santos, P. Patté, and F. Parente, At. Data Nucl. Data Tables **86**, 117 (2004).
[28] V. Kaufman, J. Sugar, and W. L. Rowan, J. Opt. Soc. Am. B **5**, 1273 (1988).
[29] H. H. Hacker *et al.*, Appl. Phys. B **73**, 59 (2001).
[30] J. F. Seely, C. M. Brown, U. Feldman, J. O. Ekberg, C. J. Keane, B. J. MacGowan, D. R. Kania, and W. E. Behring, At. Data Nucl. Data Tables **47**, 1 (1991).
[31] J. Reader, V. Kaufman, J. Sugar, J. O. Ekberg, U. Feldman, C. M. Brown, J. F. Seely, and W. L. Rowan, J. Opt. Soc. Am. B **4**, 1821 (1987).
[32] J. F. Seely, J. O. Ekberg, U. Feldman, J. L. Schwob, S. Suckewer, and A. Wouters, J. Opt. Soc. Am. B **5**, 602 (1988).
[33] J. O. Ekberg, U. Feldman, J. F. Seely, C. M. Brown, B. J. MacGowan, D. R. Kania, and C. J. Keane, Phys. Scr. **43**, 19 (1991).
[34] K. N. Huang, At. Data Nucl. Data Tables **34**, 1 (1986).
[35] K. N. Huang, At. Data Nucl. Data Tables **32**, 503 (1985).
[36] K. J. Reed, M. H. Chen, and D. L. Moores, Phys. Rev. A **42**, 5315 (1990).
[37] D. Schneider *et al.*, Phys. Rev. A **42**, 3889 (1990).
[38] A. M. Howald, D. C. Gregory, F. W. Meyer, R. A. Phaneuf, A. Müller, N. Djuric, and G. H. Dunn, Phys. Rev. A **33**, 3779 (1986).